Journal of Materials Chemistry A

ROYAL SOCIETY OF CHEMISTRY

PAPER

View Article Online
View Journal | View Issue

Cite this: J. Mater. Chem. A, 2024, 12, 23461

Multinuclear solid-state NMR investigation of structurally diverse low-dimensional hybrid metal halide perovskites†

Thomas J. N. Hooper, *[a] Benny Febriansyah, [bc] Thirumal Krishnamoorthy,[d] Walter P. D. Wong, [d] Kai Xue,[e] Joel W. Ager [bf] and Nripan Mathews [cd]

Owing to their synthetic versatility and optoelectronic tunability, low-dimensional hybrid metal halide perovskites (MHPs) provide a key avenue for the design of future optoelectronic materials. Nuclear magnetic resonance (NMR) spectroscopy has emerged as a powerful tool for structural characterisation and molecular dynamics elucidation in MHPs, which are known to control the materials' optoelectronic properties. In this work, we utilise solid state NMR to study structurally diverse hybrid MHPs containing 2D, 1D and 0D inorganic motifs that are templated by a series of xylylenediammonium cations and compare their characteristics with those of archetype 3D perovskites. The highly resolved scalar coupling pattern ($J^1(^{207}Pb-^{79/81}Br) = 1.98$ kHz) in the ^{207}Pb NMR spectrum of 0D *meta*-xylylenediammonium lead bromide ($(mXDA)_2PbBr_6$), reveals that ^{207}Pb NMR of methylammonium lead bromide ($MAPbBr_3$) and formadinium lead bromide ($FAPbBr_3$) is sensitive to local Br positional disorder, associated with the fast reorientation of the MA/FA cations. Variable temperature ^{1}H spin–lattice relaxation quantifies the correlation time of the reorientation of the MA/FA cations at picosecond timescales, in contrast to the slower motion of the bulky cations in the low-dimensional perovskites. Additionally, the study of *meta*-xylylenediammonium tin halides ($(mXDA)_2SnX_6$) provides the first direct detection of tin-halide scalar coupling patterns ($J^1(^{119}Sn-^{79/81}Br) = 1.51$ kHz; $J^1(^{119}Sn-^{35/37}Cl) = 260$ Hz).

Received 24th April 2024
Accepted 25th July 2024

DOI: 10.1039/d4ta02833c

rsc.li/materials-a

Introduction

Metal halide perovskites (MHPs) have been the subject of fervent research over the last ten years due to their exceptional optoelectronic properties and flexible structural characteristics.[1,2] The typical three-dimensional (3D) crystal structure of MHPs is given by the chemical formula ABX_3, where the metal centre B^{2+} is surrounded by six halide X^- anions (chlorine, bromine or iodine) forming the octahedral repeat unit. Lead halide perovskites have, in particular, garnered the most interest due to their capability to yield high efficiency optoelectronic devices, however less-toxic alternatives have also been actively researched with tin emerging as the most promising non-lead metal centre.[3,4] The A^+ cations are typically small organic molecules, such as methylammonium (MA) and formadinium (FA), in organic–inorganic "hybrid" perovskites or small inorganic ions (Cs^+) in all-inorganic perovskites, all of which act as structural templating and charge balancing agents.

In the typical ABX_3 perovskite structures, the halometallate octahedral units are connected through corner sharing in three directions, creating 3D inorganic lattices. However, the versatile structural flexibility of the metal halide perovskite system allows different dimensional frameworks to be realised through the use of suitable larger organic cations. In contrast to morphologically controlled species (*e.g.* 2D nanoplates and 0D quantum dots), the corresponding hybrid materials feature inorganic frameworks that are of reduced dimensionality (*i.e.* limited connectivity) at the molecular level. 2D perovskites, such as butylammonium lead bromide ($(BA)_2PbBr_4$),[5] contain sheets, or layers, of typically corner sharing $[BX_6]^{4-}$ octahedra, while 1D and 0D congeners contain chains of $[BX_6]^{4-}$ octahedra and

[a]Department of Microbial and Molecular Systems (M2S), Centre for Membrane Separations, Adsorption, Catalysis and Spectroscopy for Sustainable Solutions (cMACS), KU Leuven, 3001, Belgium. E-mail: thomas.hooper@kuleuven.be
[b]Berkeley Educational Alliance for Research in Singapore (BEARS), 1 CREATE Way, Singapore 138602, Singapore
[c]Energy Research Institute at NTU (ERI@N), Research Techno Plaza, X-Frontier Block Level 5, 50 Nanyang Drive, Singapore 637553, Singapore
[d]School of Materials Science and Engineering, Nanyang Technological University, 50 Nanyang Avenue, Singapore 639798, Singapore
[e]Centre of High Field Nuclear Magnetic Resonance (NMR) Spectroscopy and Imaging, Nanyang Technological University, 21 Nanyang Link, Singapore 637371, Singapore
[f]Department of Materials Science and Engineering, University of California at Berkeley, Berkeley, California 94720, USA

† Electronic supplementary information (ESI) available. CCDC 2300670, 2300671, 2300669, 2350304, 2300668 and 1545198. For ESI and crystallographic data in CIF or other electronic format see DOI: https://doi.org/10.1039/d4ta02833c

isolated octahedral $[BX_6]^{4-}$ units, respectively. The latter generally follows the chemical formula A_4BX_6, which is identical to the 0D caesium lead bromide phase Cs_4PbBr_6.[6] Physically, the reduced dimensionality at molecular level leads to various quantum-confinement induced effects, such as tunable band gaps and improved photoluminescence, while also resulting in higher stability than their nanosized analogues. In this article, the use of 0D, 1D, and 2D terminologies shall refer to such low-dimensional hybrid perovskites.

Solid state nuclear magnetic resonance (NMR) spectroscopy has been shown to be a powerful, non-destructive technique in the structural characterisation of perovskites.[7–9] It can analyse both amorphous (surface or nanocrystal MHP) and crystalline (bulk MHP) materials, unlike traditional diffraction techniques. In addition to structural information, NMR can probe molecular dynamics and chemical bonding *via* relaxometry and correlation NMR, respectively. Furthermore, its element-specific nature allows focused investigation on the desired component (metal, ion, ligand, or dopant). The majority of NMR perovskite reports have focused on the study of cation phases, dynamics and molecular rotations in hybrid perovskites using ^{1}H, ^{2}H, ^{13}C, ^{14}N and ^{133}Cs NMR experiments.[7,10–44] In addition, ^{207}Pb NMR has been proven to be useful in determining the structure and phase composition of lead halide perovskites with new or mixed cations/anions;[31,32,36,44–68] high resolution ^{207}Pb NMR spectra of some perovskites have also revealed scalar coupling patterns.[24,31,46,47,69]

Scalar coupling (also called *J*-coupling) refers to the perturbation of the observed nuclei's energy levels due to the polarisation of the covalent bond electron pairs by a secondary nuclei. This creates a splitting in the NMR resonance, with a frequency difference equal to the scalar coupling parameter J^1. The energy level is raised or lowered depending on the orientation of the second nucleus's spin sub-level (m) with the external magnetic field. Hence, a bond to a spin S which has $2S + 1$ possible spin sub-levels, results in $2S + 1$ degenerate energy levels. The splitting of the energy levels is compounded when the observed nucleus is bonded to multiple magnetically equivalent nuclei. The final number of degenerate energy levels is given by $2nS + 1$, where n is the number of such bonds. In the NMR spectrum this manifests as a splitting of the resonance into a multiplet of $2nS + 1$ resonances, whose intensities follow a binomial distribution. The strength of the scalar coupling, quantified by J^1, is dependent on multiple factors including the degree of covalence of the bonds and the degree of orbital overlap. Hence, ^{207}Pb scalar coupling can provide information on the haloplumbate bond lengths, angles and rigidity in perovskite materials.

Recently, Aebli *et al.* measured the ^{207}Pb NMR of $MAPbX_3$, $FAPbX_3$, $CsPbX_3$ and Cs_4PbBr_6 (X = Br and Cl) and confirmed an absence of resolved scalar coupling for $MAPbBr_3$ and $FAPbBr_3$ at room temperature. This absence is intriguing as the predicted perfect cubic symmetry of the $PbBr_6$ octahedra in these perovskites rules out merging of the scalar coupling pattern due to structural asymmetry. Conversely, greater structural symmetry explains the more resolved scalar coupling pattern in Cs_4PbBr_6 than $CsPbBr_3$, which has been observed in several reports.[46,47,69] Aebli *et al.*[69] postulated that the lack of scalar coupling resolution at room temperature in $MAPbBr_3$ and $FAPbBr_3$ was result of the fast cation dynamics in both systems. Hence, ^{207}Pb NMR could prove to also be a probe of the fast organic cation dynamics in hybrid perovskites, which, outside of NMR techniques, has relied upon neutron scattering or molecular dynamic simulations for study.[18,70,71] For their hypothesis to be proven, Aebli *et al.* called for comparison with 0D hybrid perovskites. Such materials could provide a symmetric PbX_6 octahedral configuration, without the rapid cation dynamics environment, due to the significant steric effect provided by the relatively bulkier organic molecules required to template a 0D perovskite structure.

Therefore, the lead–bromide hybrid perovskite based on the *meta*-xylylenediammonium cation ($(m\text{XDA})_4PbBr_6$) was chosen for this work because it has been shown to feature relatively symmetrical $[PbBr_6]^{4-}$ octahedra in an isolated 0D structure.[72–74] We further found that by simply changing the position of the methylammonium chain, the resulting inorganic frameworks within the materials crystal lattice can be modulated. In particular, *para*-xylylenediammonium induces the formation of monolayered 2D lead bromide structure in $(p\text{XDA})PbBr_4$, while *ortho*-xylylenediammonium templates 1D bromoplumbate chain motifs in $(o\text{XDA})_2Pb_2Br_8$. As such, the XDA cation series acts as a perfect platform to study not only the scalar coupling properties and how it is related to the cation dynamics, but also to gain insight over how such properties would vary as a function of inorganic structural dimensionality.

This work presents the first ^{207}Pb MAS NMR of the xylylenediammonium lead bromides which, alongside structural data *via* single crystal X-ray diffractometry (SCXRD), is compared to well-known lead halide perovskites: $MAPbBr_3$, $FAPbBr_3$, $CsPbBr_3$, Cs_4PbBr_6 and $(BA)_2PbBr_4$. The results are corroborated with cation dynamics *via* ^{1}H/^{133}Cs spin–lattice nuclear relaxation measurements. In addition, we provide the first synthesis and structural characterisations of: *ortho*-xylylenediammonium lead bromide, $(o\text{XDA})_2Pb_2Br_8$; *meta*-xylylenediammonium lead chloride, $(m\text{XDA})_2PbCl_6$; *meta*-xylylenediammonium tin bromide, $(m\text{XDA})_2SnBr_6$; and *meta*-xylylenediammonium tin chloride, $(m\text{XDA})_2SnCl_6$. The 0D tin perovskites are also examined *via* ^{119}Sn MAS NMR experiments.

Methodology

Synthetic procedures

Growth of single crystals of $MAPbBr_3$, $FAPbBr_3$, $CsPbBr_3$, Cs_4PbBr_6, and $(BA)_2PbBr_4$. $MAPbBr_3$ and $FAPbBr_3$ samples were grown using inverse temperature crystallization.[75] Briefly, MABr (0.112 g) and $PbBr_2$ (0.367 g) were dissolved in DMF (1 mL) while FABr (0.125 g) and $PbBr_2$ (0.367 g) were dissolved in DMF–GBL (1 : 1 volume ratio total 1 mL) to create 1 M perovskite solutions. The solutions were then slowly heated to 100 °C. The resulting single crystals grown thereof were then harvested, washed and

dried under reduced pressure accordingly. Meanwhile, $CsPbBr_3$, Cs_4PbBr_6 and $(BA)_2PbBr_4$ were synthesized through the normal temperature crystallization method with concentrated HBr (48%; 1 mL)) being used as the solvent. Therein, a stochiometric amount of PbO (0.223 g) was dissolved in HBr before CsBr (0.213 g or 0.852 g)) or butylamine (0.200 mL) were added to create 1 M perovskite solutions. The solution was then heated gently to 100 °C with vigorous stirring (50 °C for Cs_4PbBr_6 with 12 hours of stirring). The solutions were then slowly cooled to room temperature to obtain crystals. The crystals were then washed and dried under reduced pressure, before being ground to fine powder for solid state NMR measurement.

General procedure for preparation of xylylenediammonium halide (XDABr/XDACl) salts. To a round bottom flask containing ethanol (~10 mL) and the requisite xylylenediamine (3.7 mmol; *ca.* 0.5 g scale), cooled to 0 °C, was added a stoichiometric amount of concentrated HBr (48%)/HCl (37%) (415/301 μL). After stirring the solution for 1 hour, all volatiles were then removed using a rotary evaporator. The solids, thereby, obtained were washed with copious amounts of diethyl ether and dried under vacuum at 50 °C overnight. (*o*XDA)Br was synthesised in inert conditions *via* the Schlenk line technique due to instability in ambient air.

Growth of single crystals of 0D (mXDA)$_2$BX$_6$ perovskites. Previously synthesized organic halide salts (in excess) were dissolved in DMF with halide salts $PbBr_2$/$PbCl_2$/$SnBr_2$/$SnCl_2$ at 100 °C (to produce a 1 M perovskite solution. Then, following the antisolvent vapour-assisted recrystallisation method, antisolvent vapour diethelether was allowed to diffuse into the perovskite solution under inert conditions, which afforded single crystals suitable for X-ray crystallography. The same crystals were stored in inert conditions before being quickly ground to fine powder and packed for solid state NMR measurement.

Growth of single crystals of (pXDA)PbBr$_4$ and (oXDA)$_2$Pb$_2$Br$_8$. The prior synthesis did not produce (pXDA)$PbBr_4$ and (oXDA)$_2Pb_2Br_8$; instead the following alternative procedure was used. Mixtures of stoichiometric amounts of organic bromide salt (synthesized previously) and $PbBr_2$ (0.25 mmol scale) in concentrated HBr (48%; 1 mL) (to produce concentrations of 0.25–0.30 M relative to Pb^{2+}) were prepared in a two-necked round bottom flask and heated, with stirring, at ~135 °C for around 1 hour. The clear solutions that resulted were then allowed to cool slowly to room temperature, which afforded single crystals suitable for X-ray crystallography. The same crystals were stored in inert conditions before being quickly ground to fine powder and packed for solid state NMR measurement.

Analytical techniques

For single crystal X-ray measurement and study, a Bruker X8 CCD area detector diffractometer was used and the data was collected using graphite monochromated Mo-Kα radiation (λ = 0.71073 Å) at particular temperatures. Data reduction and absorption corrections were performed using the SAINT and SADABS software packages, respectively.[76] All structures were solved by direct methods and refined by full-matrix least squares procedures on F2, using the Bruker SHELXTL-2014 software package.[77,78] Non-hydrogen atoms were anisotropically refined before hydrogen atoms were introduced at calculated positions for further refinement of data. The graphical illustrations of crystal structures used throughout were mainly created using the program VESTA.[79] Full crystallographic and refinement data can be found in the ESI Tables S1 and S2.†

The photoluminescence (PL) spectra were acquired using a WITec alpha 300RAS confocal Raman microscope. The UV line of a linearly polarized CW solid laser (He–Cd, 325 nm) was chosen and the excitation power was kept below 10 μW on sample to avoid photo degradation and saturation of the detector.

Solid-state NMR experiments were completed on a 14.1 T Bruker Advance III HD 600 MHz spectrometer using a 1.9 mm Bruker HXY probe. Single crystal samples were manually ground before packing. The ^{207}Pb NMR ($\nu_0(^{207}Pb)$ = 125.60 MHz) Hahn-echo experiments utilised an MAS frequency of 12 kHz, a $\pi/2$ pulse of 5 μs (determined on $Pb(NO_3)_{2(s)}$), a recycle delay of 5 s, and a rotor synchronised echo delay. The ^{1}H NMR saturation recovery experiments utilised MAS frequencies of 12–40 kHz, a ^{1}H $\pi/2$ pulse length of 2.5 μs, and a 200 pulse saturation block. The ^{119}Sn[^{1}H] and ^{13}C[^{1}H] NMR CP experiments utilised an MAS frequency of 12 kHz, a 5000 μs contact pulse length, a ^{1}H $\pi/2$ pulse length of 2.5 μs, high power proton decoupling and recycle delays dependent on the ^{1}H saturation recovery results. All spectra were processed using the Topspin software package and referenced to the unified scale using IUPAC recommended frequency ratios relative to the ^{13}C adamantane$_{(s)}$ methylene resonance (δ = 37.77 ppm).[80,81] Spectral deconvolution was performed with dmfit.[82]

Results and discussion

Each of the XDA-based materials crystallize in monoclinic space group $P2_1/c$, as determined *via* SCXRD, and the refined structures are shown in Fig. 1. Fig. 1(a–c) demonstrates how varying the position of the methylammonium functional groups on the phenyl ring of the cations results in lead bromide perovskites of different dimensionalities. In particular, mXDA leads to (mXDA)$_2PbBr_6$, a 0D perovskite with isolated octahedral units (Fig. 1(a)), while the isomeric pXDA templates the formation of (pXDA)$PbBr_4$, a 2D perovskite with isolated monolayers of corner-sharing octahedral units expanding in the b–c plane (Fig. 1(c)). The oXDA cation, on the other hand, produces (oXDA)$_2Pb_2Br_8$, which has a more complex structure, with 1-D chains of edge-sharing octahedral units along the c-axis with additional branches of singular corner-sharing units (Fig. 1(b)). Isovalent substitution of the metal halide components does not typically alter the resulting inorganic framework configuration. This is illustrated by examples shown in Fig. 1(d–f) where hybrid materials (mXDA)$_2PbCl_6$, (mXDA)$_2SnBr_6$, and (mXDA)$_2SnCl_6$ were found to exhibit the same isolated 0D structure as (mXDA)$_2PbBr_6$. To confirm the organic cation integrity in the

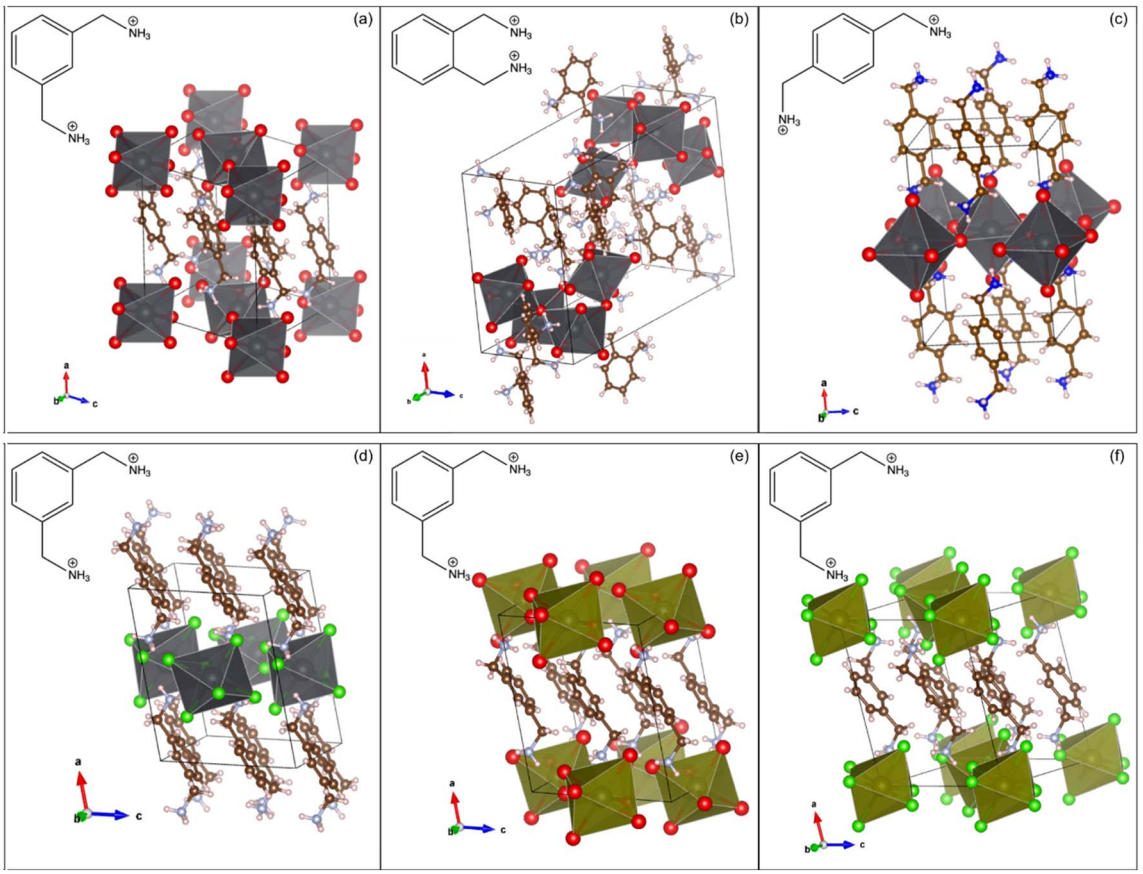

Fig. 1 The SCXRD determined structures of (a) $(m\text{XDA})_2\text{PbBr}_6$, (b) $(o\text{XDA})_2\text{Pb}_2\text{Br}_8$, (c) $(p\text{XDA})\text{PbBr}_4$, (d) $(m\text{XDA})_2\text{PbCl}_6$, (e) $(m\text{XDA})_2\text{SnBr}_6$, and (f) $(m\text{XDA})_2\text{SnCl}_6$ with molecular drawings of the respective organic cations inset.

series of low-dimensional hybrid perovskites investigated in this work, ^{13}C CPMAS NMR experiments were conducted and the corresponding spectra can be seen in ESI Fig. S1.†

Hybrid materials with isolated $[\text{PbBr}_6]^{4-}$ ions, such as 0D $(m\text{XDA})_2\text{PbBr}_6$, are relatively rare in occurrence with less than ten compounds being reported so far in the literature.[83–89] The organic species responsible for directing such molecular lead-bromide octahedra are diverse in structure, but some similarities can still be drawn. This includes the presence of both dicationic ammonium groups and a bulky core. The former is needed to not only satisfy the charge balancing requirements to the $[\text{PbBr}_6]^{4-}$ units, but also to drive the lattice formation through H bonding with Br^- ions. The relative position of the ammonium groups in the organic molecule dictates the formation of isolated $[\text{PbBr}_6]^{4-}$ octahedra. For example, a 1D chain was obtained in the case of $(o\text{XDA})_2\text{Pb}_2\text{Br}_8$ because the proximity of the methylammonium functionality in *o*XDA prevents the formation of separate octahedra. On the other hand, the ammonium groups in *p*XDA are far enough apart to allow one bromoplumbate octahedron to corner-share with four octahedral neighbors along an equatorial plane. Propagation in two directions eventually leads to layered $[\text{PbBr}_4]^{2-}$ architectures in $(p\text{XDA})\text{PbBr}_4$. The bulky core of the organic cation enforces the physical separation between each bromoplumbate octahedron as a result of steric hindering and in the case of XDA, this role is fulfilled by the phenyl ring. In all the investigated *m*XDA templated perovskites, the phenyl rings are arranged in parallel displaced stacks with centroid–centroid distances of 4.2–4.3 Å and centroid normal-centroid vector angles of 33–38°. The phenyl rings in $(p\text{XDA})\text{PbBr}_4$ and $(o\text{XDA})_2\text{Pb}_2\text{Br}_8$ are T-stacked and parallel displaced respectively (centroid–centroid distance of 5.8 and 5.4 Å). A more detailed discussion on the specificity of isomeric XDA cations in templating low-dimensional perovskite with different inorganic architectures, in comparison to other reported 0D templating cations, can be found in the ESI.†

Low-dimensional lead halide perovskites tend to demonstrate broadband photoluminescence. Such behaviour has been documented by several studies and the origin is ascribed to the self-trapped excitons formed in the disordered crystal lattice.[90–92] Structurally, the broadband emission has also been correlated with different parameters of inorganic lattice distortion within the materials, such as inter-octahedral tilting and intra-octahedral (coordination) deformation.[93–95] As expected from the octahedral distortion of the XDA lead bromide perovskites, they produce broadband emission across the visible light region (Fig. S5†).

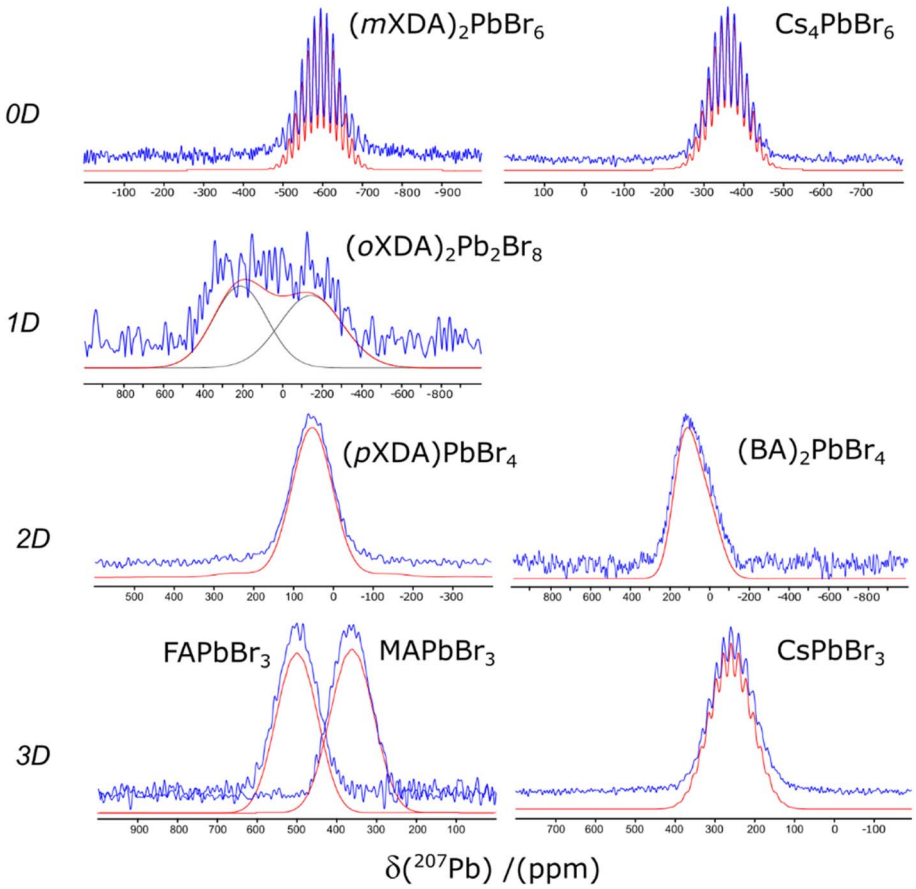

Fig. 2 The ^{207}Pb NMR spectra of the lead bromide perovskites. Experimental and simulated spectra are displayed in blue and red respectively.

The ^{207}Pb solid state NMR spectra of each lead bromide perovskite are presented in Fig. 2. Scalar coupling patterns have been resolved in the spectra of $(m\text{XDA})_2\text{PbBr}_6$, Cs_4PbBr_6, and CsPbBr_3, where coupling of ^{207}Pb nuclei (spin $\frac{1}{2}$) with six $^{79/81}$Br nuclei (spin $\frac{3}{2}$) results in 19 degenerate resonances with a binomial intensity distribution. Such phenomena have previously been observed for Cs_4PbBr_6, CsPbBr_3, CsPbCl_3, MAPbBr_3, and MAPbCl_3. Our results did not resolve the pattern for the MA perovskites, however previous reports of scalar coupling in the ^{207}Pb spectra of the MA-based perovskites were taken at much lower temperatures and/or lower magnetic fields, which explains the discrepancy.[69]

The ^{207}Pb NMR fitting parameters are detailed in Table 1. The isotropic chemical shift (δ_{iso}) varies between 600 and −600 ppm, and has a general dependency on the structure of the PbBr_6 octahedra. Fig. 3(a) shows a negative correlation between δ_{iso} and the mean Pb–Br bond length, giving a coefficient of determination (R^2) of 0.78. As the bond length increases

Table 1 ^{207}Pb NMR parameters of the lead bromide perovskites in comparison with their ^{1}H or ^{133}Cs longitudinal relaxation times T_1, determined at 14.1 T and at room temperature. Uncertainties are represented in italic parentheses

		^{207}Pb NMR			Cation NMR relaxation	
			Scalar coupling			
Perovskites	Dimensionalities	δ_{iso} (ppm)	$J^1(^{207}\text{Pb}–^{79/81}\text{Br})$ (kHz)	FWHM[a] (kHz)	^{1}H T_1 s	^{133}Cs T_1 s
$(m\text{XDA})_2\text{PbBr}_6$	0D	−595.0(6)	1.98(7)	1.17(7)	1.5	—
$(o\text{XDA})_2\text{Pb}_2\text{Br}_8$	1D	215(40), −142(47)	—	—	0.7	—
$(p\text{XDA})\text{PbBr}_4$	2D	53(7)	—	—	0.7	—
$(\text{BA})_2\text{PbBr}_4$	2D	83(15)	—	—	2	
MAPbBr_3	3D	358(7)	—	—	24	—
FAPbBr_3	3D	502(7)	—	—	32	—
Cs_4PbBr_6	0D	−361.1(7)	2.02(8)	1.26(8)	—	159
CsPbBr_3	3D	265(1)	2.38(14)	2.12(14)	—	200

[a] Full-width half maximum (FWHM) of observable scalar coupling resonances.

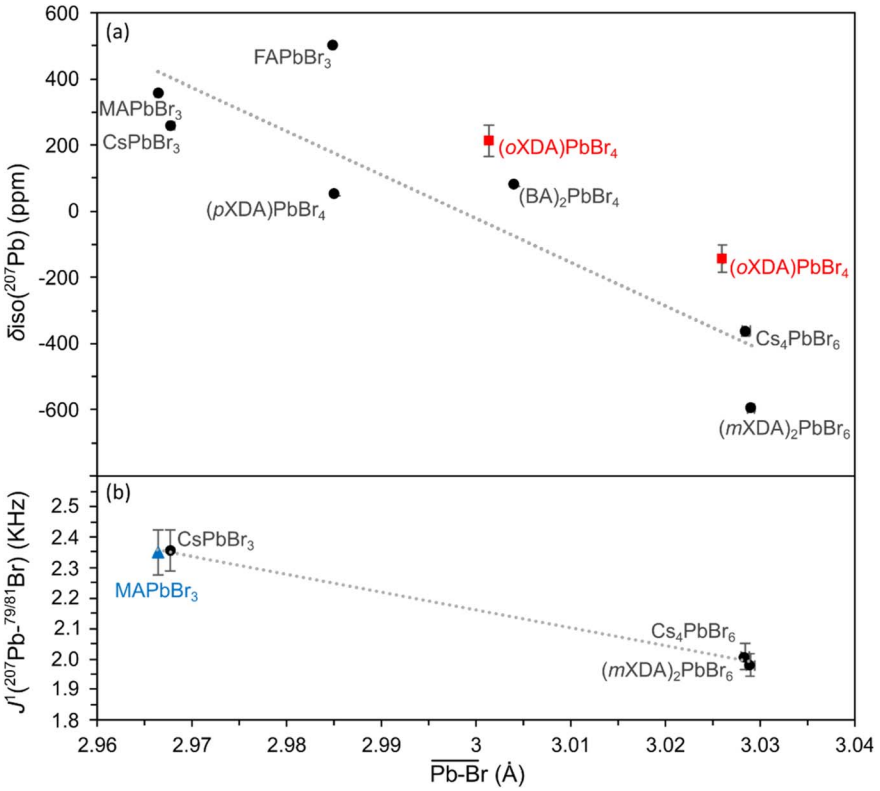

Fig. 3 Plots of (a) ^{207}Pb isotropic chemical shift and (b) ^{207}Pb–$^{79/81}$Br scalar coupling constants *vs.* octahedral Pb–Br mean atomic distance for the lead bromide perovskite series. Linear fits are presented with R^2 values of 0.776 and 0.997 for the isotropic chemical shift and scalar coupling constants respectively. Values taken from the report of Aebli *et al.*[69] are marked with blue triangles. (*o*XDA)PbBr$_4$ values are considered as anomalous (red squares) and hence are left out of the linear fits.

the negative paramagnetic shielding contribution decreases (*i.e.* the total shielding of the ^{207}Pb nucleus increases), resulting in a decrease in chemical shift frequency. This correlates with the findings of Dimitrenko *et al.* who utilised density functional theory (DFT) calculations to show that the ^{207}Pb paramagnetic contribution is the dominant variable affecting the ^{207}Pb chemical shielding when varying the electronegativity of the halide bond, achieved by swapping the *X* halide in Pb(II)X_2 compounds.[100] In addition, Lee *et al.* reported a negative correlation between δ_{iso}(^{207}Pb) and mean Pb–I bond lengths across a series of 3D/2D lead iodide perovskites.[61] Values for the two (*o*XDA)$_2$Pb$_2$Br$_8$ Pb sites were not included in the linear fit due to the large site disorder. Both sites have effective coordination numbers (n_e) below 5.7 (while sites from all other lead bromides have $n_e > 5.99$) which would strongly effect their ^{207}Pb chemical shift. Variations from the predicted trend can be explained by cation differences and distances between octahedral layers. For example, (*p*XDA)PbBr$_4$ and (BA)$_2$PbBr$_4$ have very similar structures and cations but fall on either side of the trendline. This is due to the greater inter-octahedral Pb–Pb distance in the latter (between both adjacent Pb and Pb in separate layers) resulting in a reduced magnetic shielding and hence a relatively higher chemical shift. Fig. 3(a) demonstrates how ^{207}Pb NMR can differentiate between the structural dimensionalities of the perovskites due to its sensitivity to Pb–Br bond lengths and greater structure.

The scalar coupling parameter J^1(^{207}Pb–$^{79/81}$Br) is the frequency difference between each resonance in the pattern, and is a measure of the intensity of the local magnetic field perturbation created by the shared electrons. It follows that the J^1 value for a set pair of nuclei is negatively proportional to the bond length *l*. Fig. 3(b) confirms the trend for J^1(^{207}Pb–$^{79/81}$Br) in lead bromide perovskites providing the correlation:

$$J^1 = 19.6 - 5.8\left(\overline{\text{Pb} - \text{Br}}\right) \quad (1)$$

The lead bromide perovskites investigated in this study only provided 3 data points for analysing the scalar coupling, however the J^1 value for MAPbBr$_3$ at 100 K by Aebli *et al.* also fits the trend.[69] Furthermore, the same trend can be observed for lead chloride scalar couplings, as seen in ESI Fig. S2.†

For the perovskites whose scalar coupling is not resolved, other interactions must be broadening the individual resonances sufficiently to "smear" the scalar coupling pattern. The most obvious culprit would be distortion in the [PbBr$_6$]$^{4-}$ octahedral units, where asymmetry would result in large ^{207}Pb chemical shift anisotropy broadening. In more symmetrical cases differing bond-lengths and angles could result in mismatched scalar couplings for each bond and smearing of the pattern. Table 2 details the structural parameters of each of the lead bromides investigated here, with several metrics defining distortion of the [PbBr$_6$]$^{4-}$ octahedra.

Table 2 Structural parameters of the lead bromide perovskites determined *via* SCXRD. Uncertainties are represented in italic parentheses

			Pb–Br length				
Perovskites	Dimensionality	Space group	Mean (Å)	σ (Å)	Br–Pb–Br angle variance (°)	$[PbBr_6]^{4-}$ n_e[a]	Ref.
$(m\text{XDA})_2PbBr_6$	0D	$Pm2_1/c$	3.0290(4)	0.0148	36.72	5.996	[b]
$(o\text{XDA})_2Pb_2Br_8$	1D	$Pm2_1/c$	3.0259(1), 3.0013(1)	0.1145, 0.1056	99.56, 27.56	5.671, 5.688	[b]
$(p\text{XDA})PbBr_4$	2D	$Pm2_1/c$	2.9966(3)	0.0132	6.14	5.996	[b]
$(BA)_2PbBr_4$	2D	*Pbca*	3.0040(3)	0.0078	9.42	5.999	93
$MAPbBr_3$	3D	$Pm\bar{3}m$	2.9664(3)	0.0000	0.00	6.000	96
$FAPbBr_3$	3D	$Pm\bar{3}m$	2.9849(1)	0.0000	0.00	6.000	97
Cs_4PbBr_6	0D	$R\bar{3}c$	3.0284(4)	0.000	0.06	6.000	98
$CsPbBr_3$	3D	*Pbnm*	2.9677(1)	0.0120	34.84	5.997	99

[a] Effective coordination number. [b] Determined in this work.

The 2D and 1D perovskites have ^{207}Pb patterns defined by chemical shift anisotropy (CSA) broadening due to the low symmetry about the $[PbBr_6]^{4-}$ octahedral units, which hides any underlying scalar coupling. The large Pb–Br length/angle distortion present in the two distinct lead sites in $(o\text{XDA})_2Pb_2Br_8$ (see Table 2) results in two very broad overlapping resonances. The ^{207}Pb NMR spectrum is of poor quality as the $(o\text{XDA})_2Pb_2Br_8$ perovskite was not stable and samples degraded, despite synthesizing under inert conditions and packing quickly. During the long acquisition time necessary for wide-line ^{207}Pb NMR experiments the ^{207}Pb resonance was lost and the sample had changed colour to black. The "step-like" 2D perovskite architecture reported by Hoffman *et al.*, has a similar arrangement of corner sharing $[PbX_6]^{4-}$ in shorter chains (2–4 octahedral units) which are linked by edge sharing $[PbX_6]^{4-}$ into a larger 2D network.[101] The edge sharing octahedral units in these step-like perovskites are similarly distorted as in $(o\text{XDA})_2Pb_2Br_8$, due to the asymmetrical positioning of neighbouring $[PbX_6]^{4-}$ octahedra. They reported no such problems with stability. Instead the organic molecule itself seems to be the source of the instability as the synthesized organic bromide salt degraded when left in open atmosphere. As this study was most interested in comparing the ^{207}Pb NMR of different hybrid perovskite architectures with symmetrical octahedral units, higher quality ^{207}Pb NMR of $(o\text{XDA})_2Pb_2Br_8$ was not pursued further.

The 2D perovskites $(p\text{XDA})PbBr_4$ and $(BA)_2PbBr_4$ have relatively symmetrical $[PbBr_6]^{4-}$ units ($n_e > 5.99$) so the source of the asymmetry is less obvious. In contrast, other well-known 2D lead bromide perovskites such as phenylethyl ammonium lead bromide, $(PEA)_2PbBr_4$, have more distorted octahedra (n_e = 5.76)[102] resulting in broad CSA patterns in the ^{207}Pb spectrum (see ESI Fig. S3†), which is why this perovskite was not chosen for further comparison. Instead the ^{207}Pb NMR of $(p\text{XDA})PbBr_4$ and $(BA)_2PbBr_4$ is sensitive to the asymmetry beyond their octahedral units, due to their planar arrangement of octahedra. The resulting CSA broadening is evident from the asymmetrical line-shape of the ^{207}Pb resonances, most obvious in the static spectra of $(BA)_2PbBr_4$. Their CSA fitting and parameters can be seen in ESI Fig. S3.†

The scalar coupling of $CsPbBr_3$ and Cs_4PbBr_6 have been reported several times,[14,46,69] and the poorer resolution of the pattern in $CsPbBr_3$ is due to its Pb–Br bond length variation, in contrast to the perfect symmetry of the Cs_4PbBr_6 units. The 0D and 3D hybrid perovskites are more intriguing, as a very well defined scalar coupling pattern is present in the ^{207}Pb NMR spectrum of $(m\text{XDA})_2PbBr_6$ but not present in $MAPbBr_3$ or $FAPbBr_3$ (at room temperature). This is despite the perfect symmetry in the $[PbBr_6]^{4-}$ units of the cubic 3D perovskites reported by SCXRD. By utilising the linear trend from the resolved scalar coupling patterns we can predict J^1 values for the cubic lead bromides as ~2.3 kHz, which is in agreement with the J^1 observed by Aebli *et al.* for $MAPbBr_3$ at 100 K.[69] By simulating the ^{207}Pb NMR line shapes with these J^1 values, a minimum scalar coupling resonance broadening required to obscure their patterns is determined as > 3.0 kHz. This broadening is almost triple the width of the $(m\text{XDA})_2PbBr_6$ scalar coupling resonances, despite the larger Pb–Br bond length/angle variance (see Table 2) present in the 0D perovskite.

Aebli *et al.* postulated that the lack of scalar coupling resolution in $MAPbBr_3$ and $FAPbBr_3$ at room temperature was result of the fast cation dynamics in both systems.[69] The organic cations in $MAPbX_3$ and $FAPbX_3$ are known to undergo rapid reorientation within the cuboctahedral cage. The MA and FA cation reorientation time have been thoroughly examined in the literature, providing values ranging between 0.2–5 ps for $MAPbBr_3$,[16,19,31,70,71,103,104] 6 ps for $FAPbBr_3$,[70] 0.4–14 ps for $MAPbI_3$,[16,19,34,103–107] and 2–8 ps for $FAPbI_3$.[18,34,108,109]

Evidence for Aebli and coworker's hypothesis includes the observation of a scalar coupling pattern in the ^{207}Pb NMR of $MAPbBr_3$ at 100 K, where the fast reorientation of the MA cation is reportedly much reduced.[69,70] Here, we utilised variable temperature ^{1}H NMR spin–lattice relaxation measurements to probe the cation dynamics, as reported previously for MA and FA perovskites.[16,18,110] Spin–lattice NMR relaxation (measured by the characteristic relaxation time T_1) is the return of the nuclear magnetisation to equilibrium parallel with the applied static magnetic field. In solids where the dominant relaxation occurs through the dipole–dipole interaction mediated by molecular motions,[111] the relaxation is dependent on the corelation time *via* eqn (2):

$$\frac{1}{T_1} = \frac{3\mu_0^2\hbar^2\gamma^4}{160\pi^2 r^6}\left(\frac{\tau_c}{1+\omega_0^2\tau_0^2} + \frac{4\tau_c}{1+\omega_0^2\tau_0^2}\right) \quad (2)$$

where τ_c is the correlation time of molecular reorientation and r is the inter-moment distance. This relationship is demonstrated in Fig. 4(a). The relaxation is most efficient when the molecular dynamics are at a rate close to the nuclear magnetic precession frequency ($\omega_0\tau_c \approx 1$); for ^{1}H nuclei at 14.1 T this corresponds to a τ_c around 10^{-10} s. Faster and slower molecular dynamics both result in slower relaxation. However, by observing the trend in relaxation time with temperature, which acts to increase the frequency of the molecular motion, we can determine whether the motion is in a fast ($\omega_0\tau_c \ll 1$) or slow ($\omega_0\tau_c \gg 1$) timescale regime.[18,112]

Fig. 4(b) shows the ^{1}H spin–lattice relaxation times at varying temperatures for the organic cation lead bromides. $MAPbBr_3$ and $FAPbBr_3$ have high ^{1}H T_1 relaxation times, which increase with temperature and therefore are in the fast-timescale regime at room temperature, as expected from the reported picosecond reorientation times. In the fast time scale regime ($\omega_0\tau_c \ll 1$) eqn (2) can be simplified to:

$$\tau_c = \frac{160\pi^2 r^6}{15\mu_0^2\hbar^2\gamma^4}\,\frac{1}{T_1} \quad (3)$$

Hence, by utilising the inter-moment distances determined by Fabini *et al.* for the cations in $MAPbI_3$ and $FAPbI_3$,[18] we can determine the MA and FA correlation times as 2 ps and 7 ps respectively in $MAPbBr_3$ and $FAPbBr_3$. These values are based on many assumptions and therefore should be used to judge the scale of the rate of motion, however they are in good agreement with the reported values for $MAPbBr_3$ and $FAPbBr_3$ which utilised a variety of techniques including: ^{2}H and ^{14}N quadrupolar relaxation;[19,31] quasi-elastic neutron scattering;[70] GHz spectroscopy;[103] 2D infrared spectroscopy;[104] molecular dynamics;[71] and ^{1}H nuclear relaxation.[106]

Conversely, the 0D perovskite $(m\text{XDA})_2PbBr_6$ demonstrates ^{1}H T_1 relaxation times that become shorter with increasing temperature, putting it within the slow timescale regime ($\tau_c \gg 100$ ps). By observing the perovskites ^{1}H relaxation over a wide enough temperature range to cover the entire behaviour shown in Fig. 4(a) and fitting the data with eqn (2), a more exact correlation time could be acquired. Unfortunately, we could not access a large enough temperature range for this study. However, we can confirm the intuitive hypothesis that the bulky cations forming the low dimensional perovskites are much less mobile than the rapidly reorientating cations in the 3D perovskite.

Aebli *et al.* postulated that the rapid reorientation of the cations, causes a local variation of Pb–Br bond lengths/angles in

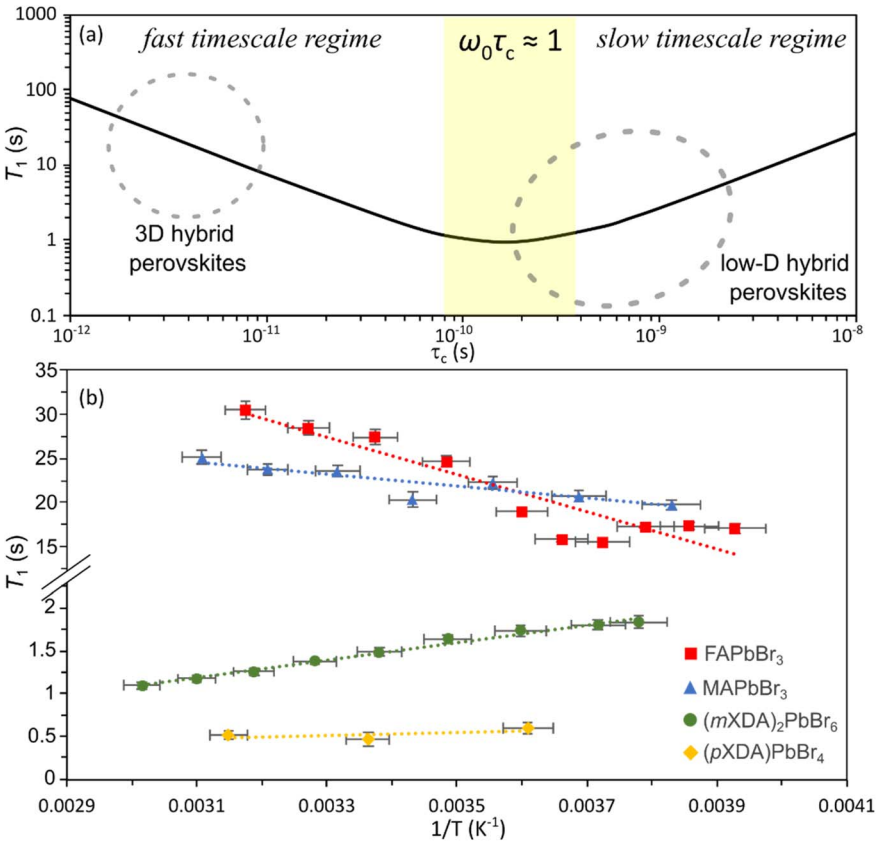

Fig. 4 (a) Schematic of the ideal ^{1}H T_1-correlation time relationship for dipolar mediated relaxation following eqn (2) at 14.1 T, using a representative inter-moment distance $r = 2$ Å, to demonstrate the different timescale regimes. (b) Plot of ^{1}H T_1 *versus* inverse temperature for $FAPbBr_3$, $MAPbBr_3$, $(m\text{XDA})_2PbBr_6$, and $(p\text{XDA})PbBr_4$.

$MAPbBr_3$ and $FAPbBr_3$, due to the H-bonding between the cation NH_3^+ groups and the surrounding Br atoms. The resulting distribution of scalar coupling strengths, J, would smear the scalar coupling pattern.[69] Our examination of a 0D hybrid lead bromide gives us a lower bound on the necessary Pb–Br distortion, as $(m\text{XDA})_2PbBr_6$ presents a well-resolved scalar coupling pattern despite a permanent Pb–Br bond length standard deviation of 0.015 Å. Additionally, the distortion cannot be only present at the picosecond timescales of the cation dynamics, otherwise the ^{207}Pb nucleus would observe an averaged Br position. Two discrete NMR resonances separated by a frequency of $\Delta\nu$ will merge when the exchange rate between the two sites becomes proportional to the reciprocal of the frequency difference. Much faster site exchange will result in the detection of a single resonance, as the NMR detection is observing the average of the two sites.[112] The necessary broadening to merge the ^{207}Pb scalar coupling patterns is ~3.0 kHz, hence dynamic disorder would need to occur at slow dynamics (>10^{-4} s timescales) to cause the required NMR line shape coalescence.

Hence, we believe the ^{207}Pb NMR scalar coupling provides further evidence of permanent short-range disorder in the local structures of $MAPbBr_3$ and $FAPbBr_3$, despite the long-range periodic cubic structure observed by SCXRD. This corroborates previous studies of $MAPbBr_3$ and $FAPbBr_3$ at room temperature showing non-cubic refinements of pair distribution function (PDF) data at <10 Å and large atomic displacement parameters (ADP) for Br perpendicular to the Pb–Br bond.[113–118] Worhatch *et al.* used X-ray PDF refinement to show improved fits in cubic 2 × 2 × 2 supercells of $MAPbBr_3$ and $FAPbBr_3$ with Br atoms displaced transversely to the Pb–Pb line, resulting in a distribution of Br–Pb–Br bond angles below 180°.[116] This transverse Br distortion is corroborated by the *ab initio* molecular dynamics studies of Maity *et al.* who showed that MA cation dynamics were correlated with Br–Pb–Br scissoring distortions.[71] Alternatively, X-ray PDF refinements by Page *et al.* and extended absorption fine structure (EXAFS) refinements by Nandi *et al.* both found improved fitting of the local structure of $MAPbBr_3$ *via* pseudo-cubic orthorhombic structures, with Pb–Br bond length standard deviations of 0.0624 and 0.164 Å respectively.[113,115] Clearly the exact local structure of the PbX_6 octahedra in hybrid 3D perovskites is still uncertain, but there is agreement on the presence of local disorder in these structures. Hence, our ^{207}Pb NMR comparison with low-dimensional hybrid perovskites confirms the presence of significant local disorder at slow timescales in $MAPbBr_3$ and $FAPbBr_3$, and corroborates the linkage between this disorder and the fast dynamics of their organic cations.

Other possible causes of the ^{207}Pb NMR broadening in $MAPbBr_3$ and $FAPbBr_3$ were investigated. Ionic diffusion in $MAPbX_3$ and $FAPbX_3$ is known to be prevalent and dominated by anion vacancy diffusion with large reported diffusion coefficients.[119–121] Despite this, the concentration of halide vacancies and mobile halides, reported to be between 10^{14}–10^{17} cm^{-3},[121–123] is too low to distort the environment of sufficient Pb nuclei to smear the bulk ^{207}Pb NMR pattern. Additionally, the halide positional exchange in MHPs is predicted to occur at the frequency of the ionic lattice vibrations (ps timescales),[120,121,124] which are too fast be the cause of the scalar coupling smearing. Dominant broadening *via* dipolar or CSA interactions can be ruled out with comparison of ^{207}Pb NMR spectra performed at variable MAS frequencies, which showed no difference in the $MAPbBr_3$ line shape between 24 kHz and static conditions (see ESI Fig. S4†). Previous reports by Rosales *et al.* and Bernard *et al.* proposed scalar relaxation due to the fast quadrupolar relaxation of the halides as the source of the ^{207}Pb NMR broadening in the lead bromides.[31,125] A spin $\frac{1}{2}$ nuclei I coupled to a fast relaxing quadrupolar nuclei S, will gain a contribution to its relaxation if the relaxation of S is at an equivalent or higher rate than the frequency of the scalar coupling parameter. This relaxation is termed scalar relaxation of the second kind (SC2) by Abragam *et al.*[126] To test this hypothesis, the ^{207}Pb T_2 relaxation of $MAPbBr_3$ was measured *via* CPMG pulse sequence. The T_2 of 0.23(3) ms correlates to a transverse relaxation broadening of 1400 Hz, close to the measured FWHM of the scalar coupling resonances in $(m\text{XDA})_2PbBr_6$ and Cs_4PbBr_6. Hence, the SC2 broadening, and other components refocused by a CPMG pulse sequence, cannot be the dominant component of the width of the ^{207}Pb resonances of $MAPbBr_3$.

Fig. 5 compares the ^{207}Pb and ^{119}Sn NMR spectra for the Br and Cl analogues of $(m\text{XDA})_2PbX_6$ and $(m\text{XDA})_2SnX_6$; the NMR parameters are presented in Table 3. The replacement of Br with Cl in $(m\text{XDA})_2PbX_6$ shifts the ^{207}Pb chemical shift by −763 ppm due to a less negative paramagnetic contribution to the chemical shielding and hence a lower chemical shift.[100] This mirrors the effect of increasing the Pb–X bond length, which was discussed previously. The same trend in ^{207}Pb δ_{iso} when changing from Br to Cl can be seen in previous reports of $MAPbX_3$, $FAPbX_3$, $CsPbX_3$, Cs_4PbX_6, and $(BA)_2PbX_4$.[45,56,58,63] Interestingly, the $\Delta\delta_{iso}$ is larger in the 3D/2D perovskites (−950 to −1000 ppm), than for the 0D perovskites $(m\text{XDA})_2PbX_6$ and Cs_4PbX_6 (−754 ppm). The difference in the scale of the trend for the 0D perovskites may be due to the longer Pb–X bond lengths, which could dampen the influence of changing the halide on the paramagnetic shielding at the Pb nucleus. This could be explored further *via* DFT calculations. The ^{119}Sn δ_{iso} of $(m\text{XDA})_2SnCl_6$ is also shifted negatively from that of $(m\text{XDA})_2SnBr_6$ (Fig. 5). Corroborating the ^{207}Pb NMR results, the ^{119}Sn $\Delta\delta_{iso}$ for the 0D mXDA perovskites is larger (−228 ppm) than that seen in the literature for 3D $MASnX_3$ perovskites (Br to Cl shift of −82 ppm).[127]

The ^{207}Pb NMR of $(m\text{XDA})_2PbCl_6$ presents with a resolved scalar coupling pattern. The $^{35/37}$Cl anions have spin $\frac{3}{2}$ like $^{79/81}$Br, resulting in the same pattern as for the lead bromides; however, the scalar coupling constant is smaller at 380 Hz (see Table 3). Furthermore, the ^{207}Pb NMR of $(m\text{XDA})_2PbCl_6$ is sufficiently resolved that it may be possible to distinguish slight differences in the resonances of ^{207}Pb coupled to ^{35}Cl and ^{37}Cl isotopes. Fig. 5 shows the two deconvoluted resonances with relative integrals equal to the natural abundance population difference between ^{35}Cl and ^{37}Cl (0.76 : 0.24); the difference in fitting quality with just one scalar coupling pattern is shown in ESI Fig. S6.† The ^{119}Sn CPMAS NMR of $(m\text{XDA})_2SnBr_6$ and $(m\text{XDA})_2SnCl_6$ (Fig. 5) demonstrates similar scalar coupling patterns to the lead bromides as ^{119}Sn is also a spin $\frac{1}{2}$ nucleus.

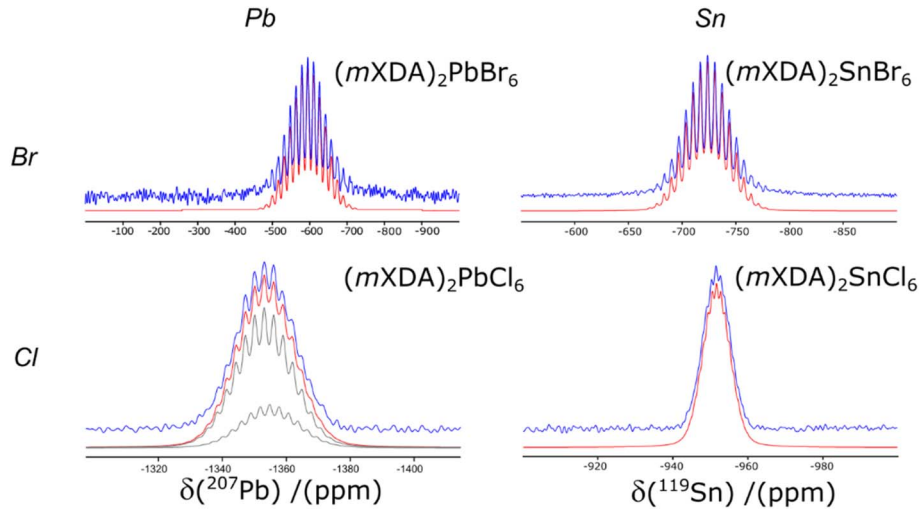

Fig. 5 The ^{207}Pb MAS NMR spectra of $(m\text{XDA})_2\text{PbBr}_6$ and $(m\text{XDA})_2\text{PbCl}_6$ and the ^{119}Sn CPMAS NMR spectra of $(m\text{XDA})_2\text{SnBr}_6$ and $(m\text{XDA})_2\text{SnCl}_6$. Experimental spectra, simulated spectra and deconvoluted resonances are displayed in blue, red and grey respectively.

Table 3 ^{207}Pb/^{119}Sn NMR parameters for $(m\text{XDA})_2BX_6$ perovskites, determined at 14.1 T and at room temperature

	^{207}Pb/^{119}Sn NMR		
		Scalar coupling	
Perovskites	δ_{iso} (ppm)	J^1(B–X) (kHz)	FWHM[a] (kHz)
$(m\text{XDA})_2\text{PbBr}_6$	−595.0	1.98	1.17
$(m\text{XDA})_2\text{PbCl}_6$	−1357.2/−1359.3	0.38/0.38	0.33/0.34
$(m\text{XDA})_2\text{SnBr}_6$	−723.8	1.50	0.80
$(m\text{XDA})_2\text{SnCl}_6$	−951.5	0.26	0.36

[a] Full-width half maximum (FWHM) of observable scalar coupling resonances.

The scalar coupling constants are reduced compared to Pb with $J^1(^{119}\text{Sn}–^{79/81}\text{Br}) = 1.51$ kHz and $J^1(^{119}\text{Sn}–^{35/37}\text{Cl}) = 260$ Hz. To the authors knowledge this is the first direct experimental observation of $J^1(^{119}\text{Sn}–^{35/37}\text{Cl})$ and $J^1(^{119}\text{Sn}–^{79/81}\text{Br})$ coupling, with previous reports providing only indirectly determined or computed values.[128,129] The resolution of scalar coupling patterns in all of the 0D perovskites despite B site metal and halide choice, corroborates the relation of the scalar coupling pattern to the rigidity of the perovskite structure. The metal halide octahedra templated by the *m*XDA cation are all relatively symmetrical with similar metrics of octahedral distortion as $(m\text{XDA})_2\text{PbBr}_6$ (see ESI Table S3†).

Conclusions

This work presents an SCXRD and solid state NMR structural characterisation of the xylylenediammonium hybrid perovskite series, which form low-dimensional 0D, 1D and 2D perovskites, due to the varying position of the NH_3 functional groups about the cations phenyl ring. Improved understanding of these structures is anticipated to assist in the design of future low-dimensional perovskites for optoelectronic perovskite applications. The *m*XDA cation is shown to form a 0D perovskite structure $(m\text{XDA})_2BX_6$ for B = Pb, Sn and X = Br, Cl. Examination of the highly resolved scalar coupling pattern present in the ^{207}Pb NMR of $(m\text{XDA})_2\text{PbBr}_6$, provides insight into the ^{207}Pb NMR of 3D perovskites MAPbBr_3 and FAPbBr_3, confirming significant local Br positional disorder coupled to the fast cation reorientation, which is not observed in the long-range averaged model provided by traditional crystallography. The local halide flexibility likely plays a role in the phenomena of halide ion migration and carrier dynamics, which are of importance to the optimal optoelectronic performance of these hybrid materials. Lastly, we further demonstrate the sensitivity of the solid state NMR toolkit to local structure and dynamics in metal halide perovskite material with diverse inorganic architectures and dimensionalities.

Data availability

Additional data supporting this article have been included as part of the ESI.† Raw NMR data for this article (Topspin data file format) are available at KU Leuven Research Data Repository at **https://doi.org/10.48804/RVHL2D**. CIF data for associated crystal structures have been deposited in the Cambridge Crystallographic Data Centre under deposition numbers CCDC 1545198, 2300668–2300671, 2350304.

Author contributions

TJNH: conception, drafting, acquisition, analysis, interpretation. BF: conception, revision, acquisition, analysis, interpretation. TK, WPDW, KX: revision, acquisition. JWA: revision. NM: conception, revision.

Conflicts of interest

The authors declare the following competing financial interest(s): N. M. is a director of Prominence Photovoltaics Pte

Ltd, a perovskite solar cell commercialization company. There are no other conflicts of interest.

Acknowledgements

We thank the Singapore Ministry of Education (Academic Research Fund MOE2019-T2-2-032), the Singapore National Research Foundation (Competitive Research Program NRF-CRP14-2014-03; Intra-CREATE Collaborative Grant NRF2018-ITC001-001; Energy Innovation Research Program NRF2015EWT-EIRP003-004; Solar CRP S18-1176-SCRP), and Fonds Wetenschappelijk Onderzoek (Senior Postdoctoral Fellowship 1253824N) for funding this research. We would like to acknowledge the Center of High Field NMR Spectroscopy and Imaging at Nanyang Technological University for the use of their facilities. In addition, TJNH is grateful for valuable discussions about the possible sources of ^{207}Pb NMR broadening with: J. V. Hanna and S. Morris, while at NTU; and D. Sakellariou and R. de Oliveira-Silva, while at KU Leuven.

Notes and references

1 S. D. Stranks and H. J. Snaith, *Nat. Nanotechnol.*, 2015, **10**, 391–402.
2 B. Saparov and D. B. Mitzi, *Chem. Rev.*, 2016, **116**, 4558–4596.
3 R. Chiara, M. Morana and L. Malavasi, *ChemPlusChem*, 2021, **86**, 879–888.
4 E. Aktas, N. Rajamanickam, J. Pascual, S. Hu, M. H. Aldamasy, D. Di Girolamo, W. Li, G. Nasti, E. Martínez-Ferrero, A. Wakamiya, E. Palomares and A. Abate, *Commun. Mater.*, 2022, **3**, 1–14.
5 D. B. Mitzi, *Chem. Mater.*, 1996, **8**, 791–800.
6 H. Lin, C. Zhou, Y. Tian, T. Siegrist and B. Ma, *ACS Energy Lett.*, 2018, **3**, 54–62.
7 L. Piveteau, V. Morad and M. V. Kovalenko, *J. Am. Chem. Soc.*, 2020, **142**, 19413–19437.
8 D. J. Kubicki, S. D. Stranks, C. P. Grey and L. Emsley, *Nat. Rev. Chem*, 2021, **5**, 624–645.
9 C. J. Dahlman, D. J. Kubicki and G. N. M. Reddy, *J. Mater. Chem. A*, 2021, **9**, 19206–19244.
10 D. J. Kubicki, D. Prochowicz, A. Hofstetter, M. Saski, P. Yadav, D. Bi, N. Pellet, J. Lewiński, S. M. Zakeeruddin, M. Grätzel and L. Emsley, *J. Am. Chem. Soc.*, 2018, **140**, 3345–3351.
11 D. J. Kubicki, D. Prochowicz, A. Hofstetter, P. Péchy, S. M. Zakeeruddin, M. Grätzel and L. Emsley, *J. Am. Chem. Soc.*, 2017, **139**, 10055–10061.
12 T. Baikie, N. S. Barrow, Y. Fang, P. J. Keenan, P. R. Slater, R. O. Piltz, M. Gutmann, S. G. Mhaisalkar and T. J. White, *J. Mater. Chem. A*, 2015, **3**, 9298–9307.
13 W. M. J. Franssen and A. P. M. Kentgens, *Solid State Nucl. Magn. Reson.*, 2019, **100**, 36–44.
14 A. Kanwat, B. Ghosh, S. E. Ng, P. J. S. Rana, Y. Lekina, T. J. N. Hooper, N. Yantara, M. Kovalev, B. Chaudhary, P. Kajal, B. Febriansyah, Q. Y. Tan, M. Klein, Z. X. Shen, J. W. Ager, S. G. Mhaisalkar and N. Mathews, *ACS Nano*, 2022, **16**, 2942–2952.
15 W. M. J. Franssen, S. G. D. van Es, R. Dervişoğlu, G. A. de Wijs and A. P. M. Kentgens, *J. Phys. Chem. Lett.*, 2017, **8**, 61–66.
16 Q. Xu, T. Eguchi, H. Nakayama, N. Nakamura and M. Kishita, *Z. Naturforsch. A*, 1991, **46**, 240–246.
17 Q. Xu, T. Eguchi and H. Nakayama, *Bull. Chem. Soc. Jpn.*, 1992, **65**, 2264–2266.
18 D. H. Fabini, T. A. Siaw, C. C. Stoumpos, G. Laurita, D. Olds, K. Page, J. G. Hu, M. G. Kanatzidis, S. Han and R. Seshadri, *J. Am. Chem. Soc.*, 2017, **139**, 16875–16884.
19 R. E. Wasylishen, O. Knop and J. B. Macdonald, *Solid State Commun.*, 1985, **56**, 581–582.
20 W. T. M. Van Gompel, R. Herckens, G. Reekmans, B. Ruttens, J. D'Haen, P. Adriaensens, L. Lutsen and D. Vanderzande, *J. Phys. Chem. C*, 2018, **122**, 4117–4124.
21 W. M. J. Franssen, B. J. Bruijnaers, V. H. L. Portengen and A. P. M. Kentgens, *ChemPhysChem*, 2018, **19**, 3107–3115.
22 C. Anelli, M. R. Chierotti, S. Bordignon, P. Quadrelli, D. Marongiu, G. Bongiovanni and L. Malavasi, *Inorg. Chem.*, 2019, **58**, 944–949.
23 D. J. Kubicki, D. Prochowicz, A. Hofstetter, S. M. Zakeeruddin, M. Grätzel and L. Emsley, *J. Am. Chem. Soc.*, 2017, **139**, 14173–14180.
24 T. J. N. Hooper, Y. Fang, A. A. M. Brown, S. H. Pu and T. J. White, *Nanoscale*, 2021, **13**, 15770–15780.
25 L. Xie, P. Vashishtha, T. M. Koh, P. C. Harikesh, N. F. Jamaludin, A. Bruno, T. J. N. Hooper, J. Li, Y. F. Ng, S. G. Mhaisalkar and N. Mathews, *Adv. Mater.*, 2020, **32**, 2003296.
26 D. Prochowicz, P. Yadav, M. Saliba, D. J. Kubicki, M. M. Tavakoli, S. M. Zakeeruddin, J. Lewiński, L. Emsley and M. Grätzel, *Nano Energy*, 2018, **49**, 523–528.
27 D. J. Kubicki, D. Prochowicz, A. Hofstetter, S. M. Zakeeruddin, M. Grätzel and L. Emsley, *J. Am. Chem. Soc.*, 2018, **140**, 7232–7238.
28 W. Xiang, Z. Wang, D. J. Kubicki, W. Tress, J. Luo, D. Prochowicz, S. Akin, L. Emsley, J. Zhou, G. Dietler, M. Grätzel and A. Hagfeldt, *Joule*, 2019, **3**, 205–214.
29 D. J. Kubicki, D. Prochowicz, A. Pinon, G. Stevanato, A. Hofstetter, S. M. Zakeeruddin, M. Grätzel and L. Emsley, *J. Mater. Chem. A*, 2019, **7**, 2326–2333.
30 O. Knop, R. E. Wasylishen, M. A. White, T. S. Cameron and M. J. M. V. Oort, *Can. J. Chem.*, 1990, **68**, 412–422.
31 G. M. Bernard, R. E. Wasylishen, C. I. Ratcliffe, V. Terskikh, Q. Wu, J. M. Buriak and T. Hauger, *J. Phys. Chem. A*, 2018, **122**, 1560–1573.
32 A. Senocrate, I. Moudrakovski and J. Maier, *Phys. Chem. Chem. Phys.*, 2018, **20**, 20043–20055.
33 A. Scarperi, N. Landi, A. Gabbani, N. Jarmouni, S. Borsacchi, L. Calucci, A. Pucci, E. Carignani, F. Pineider and M. Geppi, *Pure Appl. Chem.*, 2023, **95**, 1031–1042.
34 A. Mishra, M. A. Hope, M. Grätzel and L. Emsley, *J. Am. Chem. Soc.*, 2023, **145**, 978–990.

35 A. Mishra, D. J. Kubicki, A. Boziki, R. D. Chavan, M. Dankl, M. Mladenović, D. Prochowicz, C. P. Grey, U. Rothlisberger and L. Emsley, *ACS Energy Lett.*, 2022, **7**, 2745–2752.
36 A. Senocrate, I. Moudrakovski, G. Y. Kim, T.-Y. Yang, G. Gregori, M. Grätzel and J. Maier, *Angew. Chem., Int. Ed.*, 2017, **56**, 7755–7759.
37 P. Raval, R. M. Kennard, E. S. Vasileiadou, C. J. Dahlman, I. Spanopoulos, M. L. Chabinyc, M. Kanatzidis and G. N. Manjunatha Reddy, *ACS Energy Lett.*, 2022, **7**, 1534–1543.
38 M. A. A. Kazemi, N. Folastre, P. Raval, M. Sliwa, J. M. V. Nsanzimana, S. Golonu, A. Demortiere, J. Rousset, O. Lafon, L. Delevoye, G. N. M. Reddy and F. Sauvage, *Energy Environ. Mater.*, 2023, **6**, e12335.
39 I. Spanopoulos, I. Hadar, W. Ke, P. Guo, E. M. Mozur, E. Morgan, S. Wang, D. Zheng, S. Padgaonkar, G. N. Manjunatha Reddy, E. A. Weiss, M. C. Hersam, R. Seshadri, R. D. Schaller and M. G. Kanatzidis, *J. Am. Chem. Soc.*, 2021, **143**, 7069–7080.
40 C. J. Dahlman, R. M. Kennard, P. Paluch, N. R. Venkatesan, M. L. Chabinyc and G. N. Manjunatha Reddy, *Chem. Mater.*, 2021, **33**, 642–656.
41 A. Krishna, M. A. Akhavan Kazemi, M. Sliwa, G. N. M. Reddy, L. Delevoye, O. Lafon, A. Felten, M. T. Do, S. Gottis and F. Sauvage, *Adv. Funct. Mater.*, 2020, **30**, 1909737.
42 P. Fu, M. A. Quintero, C. Welton, X. Li, B. Cucco, M. C. De Siena, J. Even, G. Volonakis, M. Kepenekian, R. Liu, C. C. Laing, V. Klepov, Y. Liu, V. P. Dravid, G. N. Manjunatha Reddy, C. Li and M. G. Kanatzidis, *Chem. Mater.*, 2022, **34**, 9685–9698.
43 P. Raval, M. A. Akhavan Kazemi, J. Ruellou, J. Trébosc, O. Lafon, L. Delevoye, F. Sauvage and G. N. Manjunatha Reddy, *Chem. Mater.*, 2023, **35**, 2904–2917.
44 L. Pan, Z. Liu, C. Welton, V. V. Klepov, J. A. Peters, M. C. De Siena, A. Benadia, I. Pandey, A. Miceli, D. Y. Chung, G. N. M. Reddy, B. W. Wessels and M. G. Kanatzidis, *Adv. Mater.*, 2023, **35**, 2211840.
45 A. Karmakar, A. M. Askar, G. M. Bernard, V. V. Terskikh, M. Ha, S. Patel, K. Shankar and V. K. Michaelis, *Chem. Mater.*, 2018, **30**, 2309–2321.
46 A. Ray, D. Maggioni, D. Baranov, Z. Dang, M. Prato, Q. A. Akkerman, L. Goldoni, E. Caneva, L. Manna and A. L. Abdelhady, *Chem. Mater.*, 2019, **31**, 7761–7769.
47 A. Kanwat, N. Yantara, Y. F. Ng, T. J. N. Hooper, P. J. S. Rana, B. Febriansyah, P. C. Harikesh, T. Salim, P. Vashishtha, S. G. Mhaisalkar and N. Mathews, *ACS Energy Lett.*, 2020, **5**, 1804–1813.
48 M. Jagadeeswararao, P. Vashishtha, T. J. N. Hooper, A. Kanwat, J. W. M. Lim, S. K. Vishwanath, N. Yantara, T. Park, T. C. Sum, D. S. Chung, S. G. Mhaisalkar and N. Mathews, *J. Phys. Chem. Lett.*, 2021, **12**, 9569–9578.
49 B. Febriansyah, T. M. Koh, P. J. S. Rana, T. J. N. Hooper, Z. Z. Ang, Y. Li, A. Bruno, M. Grätzel, J. England, S. G. Mhaisalkar and N. Mathews, *ACS Energy Lett.*, 2020, **5**, 2305–2312.
50 B. Febriansyah, Y. Lekina, J. Kaur, T. J. N. Hooper, P. C. Harikesh, T. Salim, M. H. Lim, T. M. Koh, S. Chakraborty, Z. X. Shen, N. Mathews and J. England, *ACS Nano*, 2021, **15**, 6395–6409.
51 B. Febriansyah, Y. Li, D. Giovanni, T. Salim, T. J. N. Hooper, Y. Sim, D. Ma, S. Laxmi, Y. Lekina, T. M. Koh, Z. X. Shen, S. A. Pullarkat, T. C. Sum, S. G. Mhaisalkar, J. W. Ager and N. Mathews, *Mater. Horiz.*, 2023, **10**, 536–546.
52 P. J. S. Rana, B. Febriansyah, T. M. Koh, B. T. Muhammad, T. Salim, T. J. N. Hooper, A. Kanwat, B. Ghosh, P. Kajal, J. H. Lew, Y. C. Aw, N. Yantara, A. Bruno, S. A. Pullarkat, J. W. Ager, W. L. Leong, S. G. Mhaisalkar and N. Mathews, *Adv. Funct. Mater.*, 2022, 2113026.
53 K. Fykouras, J. Lahnsteiner, N. Leupold, P. Tinnemans, R. Moos, F. Panzer, G. A. de Wijs, M. Bokdam, H. Grüninger and A. P. M. Kentgens, *J. Mater. Chem. A*, 2023, **11**, 4587–4597.
54 B. A. Rosales, L. Men, S. D. Cady, M. P. Hanrahan, A. J. Rossini and J. Vela, *Chem. Mater.*, 2016, **28**, 6848–6859.
55 C. Roiland, G. Trippé-Allard, K. Jemli, B. Alonso, J.-C. Ameline, R. Gautier, T. Bataille, L. L. Pollès, E. Deleporte, J. Even and C. Katan, *Phys. Chem. Chem. Phys.*, 2016, **18**, 27133–27142.
56 A. Karmakar, M. S. Dodd, X. Zhang, M. S. Oakley, M. Klobukowski and V. K. Michaelis, *Chem. Commun.*, 2019, **55**, 5079–5082.
57 A. Karmakar, A. Bhattacharya, G. M. Bernard, A. Mar and V. K. Michaelis, *ACS Mater. Lett.*, 2021, 261–267.
58 A. M. Askar, A. Karmakar, G. M. Bernard, M. Ha, V. V. Terskikh, B. D. Wiltshire, S. Patel, J. Fleet, K. Shankar and V. K. Michaelis, *J. Phys. Chem. Lett.*, 2018, **9**, 2671–2677.
59 S. Brochard-Garnier, M. Paris, R. Génois, Q. Han, Y. Liu, F. Massuyeau and R. Gautier, *Adv. Funct. Mater.*, 2019, **29**, 1806728.
60 M. Aebli, B. M. Benin, K. M. McCall, V. Morad, D. Thöny, H. Grützmacher and M. V. Kovalenko, *Helv. Chim. Acta*, 2020, **103**, e2000080.
61 J. Lee, W. Lee, K. Kang, T. Lee and S. K. Lee, *Chem. Mater.*, 2021, **33**, 370–377.
62 N. Landi, E. Maurina, D. Marongiu, A. Simbula, S. Borsacchi, L. Calucci, M. Saba, E. Carignani and M. Geppi, *J. Phys. Chem. Lett.*, 2022, **13**, 9517–9525.
63 M. A. Hope, M. Cordova, A. Mishra, U. Gunes, A. Caiazzo, K. Datta, R. A. J. Janssen and L. Emsley, *Angew. Chem.*, 2024, **136**, e202314856.
64 M.-H. Tremblay, F. Thouin, J. Leisen, J. Bacsa, A. R. Srimath Kandada, J. M. Hoffman, M. G. Kanatzidis, A. D. Mohite, C. Silva, S. Barlow and S. R. Marder, *J. Am. Chem. Soc.*, 2019, **141**, 4521–4525.
65 O. Nazarenko, M. R. Kotyrba, S. Yakunin, M. Aebli, G. Rainò, B. M. Benin, M. Wörle and M. V. Kovalenko, *J. Am. Chem. Soc.*, 2018, **140**, 3850–3853.
66 P. Fu, M. A. Quintero, E. S. Vasileiadou, P. Raval, C. Welton, M. Kepenekian, G. Volonakis, J. Even, Y. Liu, C. Malliakas, Y. Yang, C. Laing, V. P. Dravid, G. N. M. Reddy, C. Li,

E. H. Sargent and M. G. Kanatzidis, *J. Am. Chem. Soc.*, 2023, **145**, 15997–16014.
67 A. Krishna, V. Škorjanc, M. Dankl, J. Hieulle, H. Phirke, A. Singh, E. A. Alharbi, H. Zhang, F. Eickemeyer, S. M. Zakeeruddin, G. N. M. Reddy, A. Redinger, U. Rothlisberger, M. Grätzel and A. Hagfeldt, *ACS Energy Lett.*, 2023, **8**, 3604–3613.
68 R. Ji, Z. Zhang, M. Deconinck, Y. J. Hofstetter, J. Shi, F. Paulus, P. Raval, G. N. M. Reddy and Y. Vaynzof, *Adv. Energy Mater.*, 2024, 2304126.
69 M. Aebli, L. Piveteau, O. Nazarenko, B. M. Benin, F. Krieg, R. Verel and M. V. Kovalenko, *Sci. Rep.*, 2020, **10**, 8229.
70 V. K. Sharma, R. Mukhopadhyay, A. Mohanty, M. Tyagi, J. P. Embs and D. D. Sarma, *J. Phys. Chem. Lett.*, 2020, **11**, 9669–9679.
71 S. Maity, S. Verma, L. M. Ramaniah and V. Srinivasan, *Chem. Mater.*, 2022, **34**, 10459–10469.
72 P. S. Klee, Y. Hirano, D. B. Cordes, A. M. Z. Slawin and J. L. Payne, *Cryst. Growth Des.*, 2022, **22**, 3815–3823.
73 T. Krishnamoorthy, *Low-dimensional metal halide perovskite phosphors for solid-state lighting*, Nanyang Technological University, 2019.
74 R. Chiara, M. Morana, G. Folpini, A. Olivati, B. Albini, P. Galinetto, L. Chelazzi, S. Ciattini, E. Fantechi, S. A. Serapian, A. Petrozza and L. Malavasi, *J. Mater. Chem. C*, 2022, **10**, 12367–12376.
75 M. I. Saidaminov, A. L. Abdelhady, G. Maculan and O. M. Bakr, *Chem. Commun.*, 2015, **51**, 17658–17661.
76 *SAINT and SADABS*, Bruker AXS Inc., 2007.
77 G. M. Sheldrick, *Acta Crystallogr., Sect. A*, 2015, **71**, 3–8.
78 G. M. Sheldrick, *Acta Crystallogr., Sect. C*, 2015, **71**, 3–8.
79 K. Momma and F. Izumi, *J. Appl. Crystallogr.*, 2011, **44**, 1272–1276.
80 R. K. Harris, E. D. Becker, S. M. Cabral De Menezes, R. Goodfellow and P. Granger, *Concepts Magn. Reson.*, 2002, **14**, 326–346.
81 R. K. Harris, E. D. Becker, S. M. Cabral de Menezes, P. Granger, R. E. Hoffman and K. W. Zilm, *Pure Appl. Chem.*, 2008, **80**, 59–84.
82 D. Massiot, F. Fayon, M. Capron, I. King, S. Le Calvé, B. Alonso, J.-O. Durand, B. Bujoli, Z. Gan and G. Hoatson, *Magn. Reson. Chem.*, 2002, **40**, 70–76.
83 Y. Takeoka, K. Asai, M. Rikukawa and K. Sanui, *Chem. Lett.*, 2005, **34**, 602–603.
84 Y. Wei, C. Li, Y. Li, Z. Luo, X. Wu, Y. Liu, L. Zhang, X. He, W. Wang and Z. Quan, *Angew. Chem., Int. Ed.*, 2022, **61**, e202212685.
85 J.-L. Song, W.-J. Chen, K.-B. Chu and Y.-H. Zhou, *Dalton Trans.*, 2018, **47**, 14497–14502.
86 B.-B. Cui, Y. Han, B. Huang, Y. Zhao, X. Wu, L. Liu, G. Cao, Q. Du, N. Liu, W. Zou, M. Sun, L. Wang, X. Liu, J. Wang, H. Zhou and Q. Chen, *Nat. Commun.*, 2019, **10**, 5190.
87 Y. Li, G. Zheng, C. Lin and J. Lin, *Solid State Sci.*, 2007, **9**, 855–861.
88 Y. Chen, Y.-Y. Zheng, G. Wu, M. Wang, H.-Z. Chen and H. Yang, *Acta Crystallogr., Sect. E: Struct. Rep. Online*, 2010, **66**, m417.
89 M.-H. Jung, K. C. Ko and W. R. Lee, *Dalton Trans.*, 2019, **48**, 15074–15090.
90 T. Hu, M. D. Smith, E. R. Dohner, M.-J. Sher, X. Wu, M. T. Trinh, A. Fisher, J. Corbett, X.-Y. Zhu, H. I. Karunadasa and A. M. Lindenberg, *J. Phys. Chem. Lett.*, 2016, **7**, 2258–2263.
91 A. Yangui, D. Garrot, J. S. Lauret, A. Lusson, G. Bouchez, E. Deleporte, S. Pillet, E. E. Bendeif, M. Castro, S. Triki, Y. Abid and K. Boukheddaden, *J. Phys. Chem. C*, 2015, **119**, 23638–23647.
92 X. Wang, W. Meng, W. Liao, J. Wang, R.-G. Xiong and Y. Yan, *J. Phys. Chem. Lett.*, 2019, **10**, 501–506.
93 M. D. Smith, A. Jaffe, E. R. Dohner, A. M. Lindenberg and H. I. Karunadasa, *Chem. Sci.*, 2017, **8**, 4497–4504.
94 B. Febriansyah, T. Borzda, D. Cortecchia, S. Neutzner, G. Folpini, T. M. Koh, Y. Li, N. Mathews, A. Petrozza and J. England, *Angew. Chem., Int. Ed.*, 2020, **59**, 10791–10796.
95 L. Mao, Y. Wu, C. C. Stoumpos, M. R. Wasielewski and M. G. Kanatzidis, *J. Am. Chem. Soc.*, 2017, **139**, 5210–5215.
96 A. Jaffe, Y. Lin, C. M. Beavers, J. Voss, W. L. Mao and H. I. Karunadasa, *ACS Cent. Sci.*, 2016, **2**, 201–209.
97 C. Li, E. J. Juarez-Perez and A. Mayoral, *Chem. Commun.*, 2022, **58**, 12164–12167.
98 M. De Bastiani, I. Dursun, Y. Zhang, B. A. Alshankiti, X.-H. Miao, J. Yin, E. Yengel, E. Alarousu, B. Turedi, J. M. Almutlaq, M. I. Saidaminov, S. Mitra, I. Gereige, A. AlSaggaf, Y. Zhu, Y. Han, I. S. Roqan, J.-L. Bredas, O. F. Mohammed and O. M. Bakr, *Chem. Mater.*, 2017, **29**, 7108–7113.
99 M. Rodová, J. Brožek, K. Knížek and K. Nitsch, *J. Therm. Anal. Calorim.*, 2003, **71**, 667–673.
100 O. Dmitrenko, S. Bai and C. Dybowski, *Solid State Nucl. Magn. Reson.*, 2008, **34**, 186–190.
101 J. M. Hoffman, X. Che, S. Sidhik, X. Li, I. Hadar, J.-C. Blancon, H. Yamaguchi, M. Kepenekian, C. Katan, J. Even, C. C. Stoumpos, A. D. Mohite and M. G. Kanatzidis, *J. Am. Chem. Soc.*, 2019, **141**, 10661–10676.
102 K. Shibuya, M. Koshimizu, F. Nishikido, H. Saito and S. Kishimoto, *Acta Crystallogr., Sect. E: Struct. Rep. Online*, 2009, **65**, m1323–m1324.
103 A. Poglitsch and D. Weber, *J. Chem. Phys.*, 1987, **87**, 6373–6378.
104 O. Selig, A. Sadhanala, C. Müller, R. Lovrincic, Z. Chen, Y. L. A. Rezus, J. M. Frost, T. L. C. Jansen and A. A. Bakulin, *J. Am. Chem. Soc.*, 2017, **139**, 4068–4074.
105 A. A. Bakulin, O. Selig, H. J. Bakker, Y. L. A. Rezus, C. Müller, T. Glaser, R. Lovrincic, Z. Sun, Z. Chen, A. Walsh, J. M. Frost and T. L. C. Jansen, *J. Phys. Chem. Lett.*, 2015, **6**, 3663–3669.
106 T. Chen, B. J. Foley, B. Ipek, M. Tyagi, J. R. D. Copley, C. M. Brown, J. J. Choi and S.-H. Lee, *Phys. Chem. Chem. Phys.*, 2015, **17**, 31278–31286.
107 A. M. A. Leguy, J. M. Frost, A. P. McMahon, V. G. Sakai, W. Kockelmann, C. Law, X. Li, F. Foglia, A. Walsh, B. C. O'Regan, J. Nelson, J. T. Cabral and P. R. F. Barnes, *Nat. Commun.*, 2015, **6**, 7124.

108 M. T. Weller, O. J. Weber, J. M. Frost and A. Walsh, *J. Phys. Chem. Lett.*, 2015, **6**, 3209–3212.
109 M. A. Carignano, Y. Saeed, S. A. Aravindh, I. S. Roqan, J. Even and C. Katan, *Phys. Chem. Chem. Phys.*, 2016, **18**, 27109–27118.
110 E. M. Mozur, M. A. Hope, J. C. Trowbridge, D. M. Halat, L. L. Daemen, A. E. Maughan, T. R. Prisk, C. P. Grey and J. R. Neilson, *Chem. Mater.*, 2020, **32**, 6266–6277.
111 N. Bloembergen, E. M. Purcell and R. V. Pound, *Phys. Rev.*, 1948, **73**, 679–712.
112 R. G. Bryant, *J. Chem. Educ.*, 1983, **60**, 933.
113 K. Page, J. E. Siewenie, P. Quadrelli and L. Malavasi, *Angew. Chem.*, 2016, **128**, 14532–14536.
114 A. Bernasconi and L. Malavasi, *ACS Energy Lett.*, 2017, **2**, 863–868.
115 P. Nandi, S. Mahana, E. Welter and D. Topwal, *J. Phys. Chem. C*, 2021, **125**, 24655–24662.
116 R. J. Worhatch, H. Kim, I. P. Swainson, A. L. Yonkeu and S. J. L. Billinge, *Chem. Mater.*, 2008, **20**, 1272–1277.
117 G. Reuveni, Y. Diskin-Posner, C. Gehrmann, S. Godse, G. G. Gkikas, I. Buchine, S. Aharon, R. Korobko, C. C. Stoumpos, D. A. Egger and O. Yaffe, *J. Phys. Chem. Lett.*, 2023, **14**, 1288–1293.
118 J.-W. Lee, S. Seo, P. Nandi, H. S. Jung, N.-G. Park and H. Shin, *iScience*, 2021, **24**, 101959.
119 A. Osherov, Y. Feldman, I. Kaplan-Ashiri, D. Cahen and G. Hodes, *Chem. Mater.*, 2020, **32**, 4223–4231.
120 J. M. Frost and A. Walsh, *Acc. Chem. Res.*, 2016, **49**, 528–535.
121 L. McGovern, M. H. Futscher, L. A. Muscarella and B. Ehrler, *J. Phys. Chem. Lett.*, 2020, **11**, 7127–7132.
122 L. Bertoluzzi, C. C. Boyd, N. Rolston, J. Xu, R. Prasanna, B. C. O'Regan and M. D. McGehee, *Joule*, 2020, **4**, 109–127.
123 H. Xue, G. Brocks and S. Tao, *Phys. Rev. Mater.*, 2022, **6**, 055402.
124 A. M. A. Leguy, A. R. Goñi, J. M. Frost, J. Skelton, F. Brivio, X. Rodríguez-Martínez, O. J. Weber, A. Pallipurath, M. I. Alonso, M. Campoy-Quiles, M. T. Weller, J. Nelson, A. Walsh and P. R. F. Barnes, *Phys. Chem. Chem. Phys.*, 2016, **18**, 27051–27066.
125 B. A. Rosales, M. P. Hanrahan, B. W. Boote, A. J. Rossini, E. A. Smith and J. Vela, *ACS Energy Lett.*, 2017, **2**, 906–914.
126 A. Abragam and A. Abragam, *The Principles of Nuclear Magnetism*, Oxford University Press, Oxford, New York, 1983.
127 D. J. Kubicki, D. Prochowicz, E. Salager, A. Rakhmatullin, C. P. Grey, L. Emsley and S. D. Stranks, *J. Am. Chem. Soc.*, 2020, **142**, 7813–7826.
128 R. R. Sharp, *J. Chem. Phys.*, 1974, **60**, 1149–1157.
129 A. Bagno, G. Casella and G. Saielli, *J. Chem. Theory Comput.*, 2006, **2**, 37–46.